Research Article

Amer S. Elameer, Mustafa Musa Jaber*, and Sura Khalil Abd

Radiography image analysis using cat swarm optimized deep belief networks

https://doi.org/10.1515/jisys-2021-0172
received August 04, 2021; accepted September 21, 2021

Abstract: Radiography images are widely utilized in the health sector to recognize the patient health condition. The noise and irrelevant region information minimize the entire disease detection accuracy and computation complexity. Therefore, in this study, statistical Kolmogorov–Smirnov test has been integrated with wavelet transform to overcome the de-noising issues. Then the cat swarm-optimized deep belief network is applied to extract the features from the affected region. The optimized deep learning model reduces the feature training cost and time and improves the overall disease detection accuracy. The network learning process is enhanced according to the AdaDelta learning process, which replaces the learning parameter with a delta value. This process minimizes the error rate while recognizing the disease. The efficiency of the system evaluated using image retrieval in medical application dataset. This process helps to determine the various diseases such as breast, lung, and pediatric studies.

Keyword: radiography images, statistical Kolmogorov–Simonov test, cat swarm-optimized deep belief networks, AdaDelta learning process.

1 Introduction

Radiography [1] is nothing but the imaging technique that utilizes the gamma, X-rays, and nonionizing and ionizing radiations to analyze and view the objects' internal structure. This radiographic process is widely applied in industrial and medical diagnostic purposes. Initially, the X-ray generators are used to pass the X-ray on items [2]. The object absorbed the specific amount of radiation (depends on the object density), and the internal structure has been viewed successfully. Among the various applications, the radiography process is widely applied in the medical sector in different formats [3,4] such as projectional radiography, computed tomography, dual-energy X-ray absorptiometry, contrast radiography, and fluoroscopy. The radiographic method is used on the human body for capturing the internal body structure and changes. The human body consists of various level substances with varying density information; therefore, nonionizing and ionizing radiations are utilized to capture the human organs [5,6]. This process is carried out by the radiographers, who are called the radiologists. The captured medical radiography images [7] are used to perform the different clinical analyses [8,9] such as dental examination, mammography analysis, orthopedics evaluation, verifying the surgical markers, spot film identification, chiropractic examination, and invasive procedure analysis. The clinical analysis process requires the radiographic or medical imaging because the healthcare specialists access the patient's organs, bones, blood vessels, and tissues via only the

* **Corresponding author: Mustafa Musa Jaber,** Department of Computer Science, Dijlah University Collage, Baghdad, 00964, Iraq; Department of Computer Science, Al-Turath University College, Baghdad, Iraq, e-mail: Mustafa.musa@duc.edu.iq
Amer S. Elameer: Biomedical Informatics College, University of Information Technology and Communications (UOITC), Baghdad, Iraq, e-mail: Amerelameer@yahoo.com
Sura Khalil Abd: Department of Computer Science, Dijlah University Collage, Baghdad, 00964, Iraq, e-mail: sura.khalil@duc.edu.iq

noninvasive technique. Only with the help of theses images, the treatment effectiveness, tumor location, blood clot identification, and other treatment procedures are handled with minimum risk [10]. Based on the discussion, here, few radiographic images are illustrated in Figure 1.

Figure 1: Sample medical radiography images.

The collected radiography images are processed by various machine learning techniques [10–13] for predicting the changes in the internal organs. However, conventional image processing techniques ensure poor performance due to inconsistent details and noisy information. Therefore, deep learning (DL) [14] concepts are widely utilized in the computer vision field to resolve the image processing problems. The traditional image analysis and machine learning techniques are mostly depending on the high number of features that require the clinical experts, labor-intensive process, and preprocessing because the experts need to know [15]. However, the DL model can catch the image features' internal and hidden representation with minimum medical experts' knowledge. Therefore, the DL process ensures superior performance although the system examines the high-dimensional and complex data analysis [16–18]. Although the DL model works effectively, the radiographic images have noisy details that cause the wrong feature extraction and pattern identification process. The false identification of image features and patterns leads to a further increase in feature training time, cost, and computation complexities. For overcoming these issues, the DL model performance should be enhanced by applying the effective optimization technique. In this article, the statistical Kolmogorov–Smirnov test (KSt) [19] has been integrated with wavelet transform to overcome the de-noising issues.

This method effectively examines every pixel in the radiographic images, and the unwanted or noise information is removed by performing the decomposition process. The features are then extracted according to the cat swarm-optimized DL model [20,21] that utilizes the various layers and learning functions to derive the image features. During the learning process, the system uses the AdaDelta learning process to enhance the network training process. Then the effective and optimized technique minimizes the deviations while deriving the medical features from the radiographic images. Finally, the same DL approach is applied to making clinical decisions. The discussed system has been implemented using the MATLAB tool, and the system uses Medical Segmentation Decathlon dataset [22]. The optimized DL model performance's effectiveness is evaluated by extracting the various medical images features and patterns with a minimum error rate and maximum accuracy metrics.

The manuscript is arranged as follows: Section 2 discusses the different research works and analyses the medical radiographic images; Section 3 explains the working process of the optimized DL model for retrieving the clinical patterns; Section 4 evaluates the excellence of the introduced system; and Section 5 defines the conclusion.

2 Related works

Pandya et al. [23] applied DL techniques for analyzing medical images and detecting diseases. This process uses the medical images (computerized tomography (CT), magnetic resonance imaging (MRI), etc.), biomedical signaling (electrocardiogram, electroencephalogram, and omics (DNA, RNA, etc.) to examine the clinical diseases. The captured medical images are processed by different DL models such as deep belief networks (DBNs), long short-term memory, stacked autoencoder, convolution networks, and recurrent networks. In addition to this, deep hybridized approaches such as multidimensional recurrent networks, deep spatiotemporal networks, and recurrent bidirectional networks classify the diseases from the medical images. Thus, the different DL model ensures promising results while analyzing the medical images with a minimum error rate and human efforts.

Debelee et al. [24] created the breast cancer medical images analyzing system using a deep learning approach (DLA). This process obtains the breast images via the magnetic resonance imaging, digital mammography, ultrasound, and breast tomosynthesis. The gathered medical images are processed using the DL model that predicts the breast cancer patterns with minimum involvement of domain experts.

Wuestemann et al. [25] examined the bone scans to diagnose the tumor entities by applying the DL-based neural network algorithm. This study uses the bone scan imaging (BSI) index values to examine the bone radiographic images. The prostate, lung, breast, and hepatocellular carcinoma cancer entities are examined using DL model from the BSI values. This process helps to minimize the working load also to improve the workflow process in the medical department.

Rehman et al. [26] implemented the brain tumor detection system using the transfer learning with deep learning framework (TLDLF), which uses three convolution networks such as VGGNet, GooglLeNet, and AlexNet for analyzing the various brain tumors such as pituitary, glioma, and meningioma. During the analysis, MRI images are examined with the help of freeze and fine-tune transfer learning process. Data augmentation techniques are applied to generalize the MRI slice image, which helps minimize data overfitting and enhance overall brain tumor recognition accuracy.

Sharma et al. [27] segmented brain tumor-affected region from MRI images using the different evaluations with the OTSU method and neural networks. Initially, in the MRI image, global threshold values are estimated to recognize the tumor-affected region. The optimal threshold value is selected according to the introduced algorithm. This process is continuously trained using neural networks, which effectively minimizes the error rate.

Abid et al. [28] identified lung cancer nodules from CT images using multiview convolution recurrent neural networks (MCRNN). This system is used to resolve the cost-intensive and inconsistent results while recognizing lung cancer nodules. The introduced method utilizes the effective learning process, which examines the image size, shape, and cross-slice variations that improve the accuracy of lung cancer identification. The system's performance was evaluated using Lung Image Database Consortium and Image database resource initiative database with the respective performance metrics.

Azizi et al. [29] examined temporal-enhanced ultrasound images for detecting prostate cancer using deep recurrent neural networks (DRNN). The introduced DRNN approach is analyzing the temporal details from ultrasound images. The extracted information is further investigated with long-term neural networks recognizing the benign and malignant with higher accuracy.

Masud et al. [30] diagnosed breast cancer from ultrasound images using convolution neural networks (CNN). Initially, the ultrasound images are trained by eight different fine-tune models that help to identify the test images related to clinical results. This process utilizes the 10-fold cross-validation process to evaluate the excellence of the system. In addition to this, various research studies are summarized in Table 1.

Table 1: Research studies on DL techniques for investigating the various medical imaging

S. no	Ref.	Year	Images	Database	Method
1	[31]	2017	Brain	2015 MICCAI Gland Segmentation Challenge and 2015 MICCAI Nuclei Segmentation Challenge	Deep contour-aware networks
2	[32]	2017	Cervix	ISBI 2015 Challenge Dataset and Shenzhen University Dataset	Multiscale deep convolutional networks
3	[33]	2017	Multiple organs	Hematoxylin and eosin (H&E)-stained tissue images	DL model
4	[34]	2018	Rat kidney	Multiple datasets	CNN
5	[35]	2019	Multiple organs	H&E-stained histopathology data	Fully CNN
6	[36]	2019	Multiple organs	2018 MICCAI challenge of Multi-Organ Nuclei-Segmentation dataset	Contour-aware informative aggregation network
7	[37]	2017	Colon histology images	2015 MICCAI Gland Segmentation Challenge	Deep multichannel neural networks
8	[38]	2018	Pulmonary	Multiple datasets	Convolutional neural networks
9	[39]	2017	Spine	1788 pairs of CT and depth images from the real clinical setting	Deep context reinforcement learning

According to the above research studies, DL techniques are widely utilized in the medical field to recognize various clinical diseases. The DL models with effective learning techniques and activation functions to identify the disease-affected region. The DL model requires the optimization process to improve the overall clinical analysis process by reducing the cost, labor intensive, and computation complexity. Moreover, the captured radiographic images are having several noises while gathering the images. Then, the de-noising process also played a crucial role while investing the medical images. So, in this article, we applied the optimized techniques to examine the different radiographic images. The detailed working process of cat swarm-optimized DBNs-based radiography image analysis is discussed in the following section.

3 Radiography image analysis using optimized DBNs

The detailed working process of optimized DBN-based radiography image analysis is explained in this section. The system aims to increase the radiography image analysis accuracy by reducing the time, error rate, and computation complexity. This process uses different steps such as image noise removal, segmentation, feature extraction, and classification process. According to the discussion, the working process is shown in Figure 2.

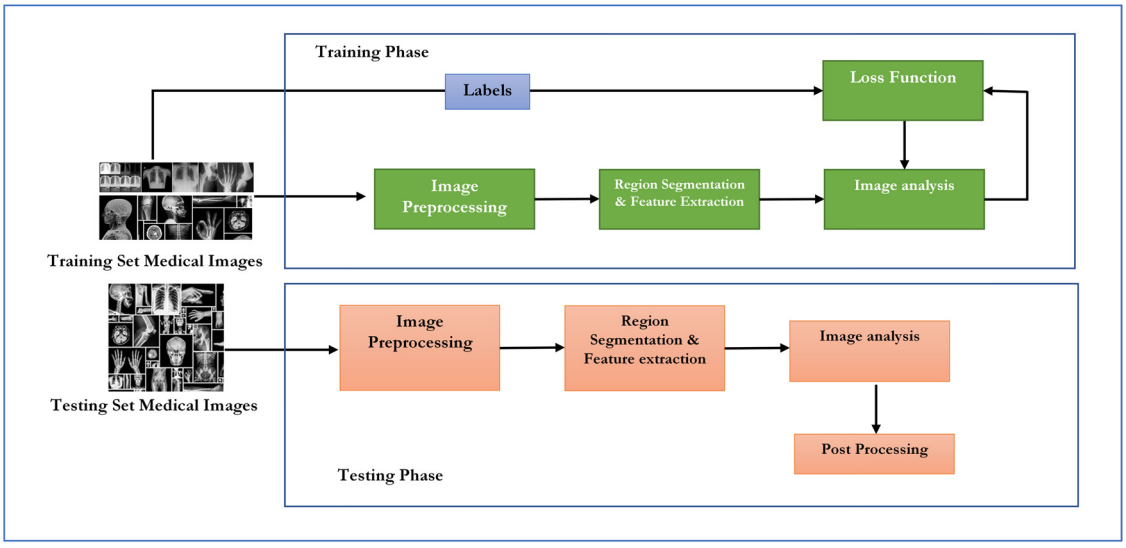

Figure 2: Radiography image analysis structure.

Radiography image analysis structure is demonstrated in Figure 2. This system uses the two phases: training and testing; each stage has image preprocessing, segmentation, feature extraction, and classification processes. The training phases use effective learning functions while deriving the medical features and classification process. During the training process, labels are provided and stored in the database. With the help of training images, testing has to be performed to identify the new image patterns. The detailed working process of radiography image analysis is discussed in the following section.

3.1 Medical image preprocessing

Preprocessing is nothing but improving the image's quality by applying statistical analysis in a comparable and repeatable manner [1,2]. In medical image processing, the noise removal process consists of

resampling, intensity normalization, and co-registration methods. These processes are more helpful to improve further radiographic image analysis. The co-registration is the way of mapping the images with respective reference coordinate system; resampling is performing the voxel size of images with the unique voxel resolution. Therefore, the collected radiographic images are resized into 160×160 dimension, and the one-row matrix need to be reshaped.

Further, the complexity of the original images has to be reduced by applying the single-level discrete two-dimensional wavelet transform approach, which examines the highly discriminative coefficient values from the medical images; the best coefficient values are selected according to the statistical KSt. Initially, the wavelet transform is applied to the image for reducing the dimensionality of the images by examining the image pixel density value. The density values are derived by using high and low pass filters. Here, Haar wavelet function is applied to the image because of the orthogonality property, which effectively examines the image wavelet coefficients. Considering the mother Haar wavelet function is $\varphi(x)$ that is defined by equation (1).

$$\varphi\left[\frac{(x-b)}{a}\right],\ (a,b) \in R^{+} \times R. \tag{1}$$

In equation (1), a and b are parameters having the value as $a = 2^{-j}$ and $b = 2^{-j}k{\cdot}k \in N$. The Haar wavelet $\varphi(x)$ dilation and translation values are estimated from equation (2) that has the orthogonal basis value as $L^2(R)$. Then, the elements presented in the orthogonal basis values are computed using equation (2).

$$\varphi_{jk}(x) = \text{const.}\quad \varphi(2^{j}x - k) \tag{2}$$

Based on equations (1 and 2), image intensity corresponding coefficient values are computed, and coefficient values are estimated. Then best coefficient values are selected according to the statistical KSt. It is one of the nonparametric tests comparing the two coefficients values from the extracted image coefficient values. This section process is performed according to the location and shape of pixels and cumulative distribution value. Then the empirical distribution function (F_n) is computed from the distributed observations X_i, which is computed using equation (3).

$$F_n(x) = \frac{1}{n}\sum_{i=1}^{n} I_{[-\inf,x]}(X_i) \tag{3}$$

In equation (3), n is independent; the indicator function is denoted as I. From the computed $F_n(x)$ value, KSt is examined using equation (4).

$$D_n = \sup_x[F_n(x) - F(x)] \tag{4}$$

In equation (4), the supremum of set distance is denoted as $\sup_x$. From the computed distance D_n value, the KSt samples are analyzed using equation (5).

$$D_n = \sup_x[F_1(x) - F_2(x)] \tag{5}$$

According to the KSt test similarity values, each pixel was examined with the alternative and null hypothesis. If the pixel has an H0 (null) hypothesis, then both pixels have the same distribution, and there is no need to replace or remove the pixel. If the pixel belongs to the alternative (H1) hypothesis, then pixel has a different population that needs to be removed from the image and replaced by using a median value. After removing the medical image's noise, the disease-affected region must be extracted according to the Prewitt kernel operator.

3.2 Region of interest (ROI) region segmentation

The next step is to extract the disease-affected region by applying the Prewitt kernel operator. This process examines the medical image regions by investigating the image edge-related features. The medical image

edge features are placed a crucial role while predicting the disease-affected region. This process works similar to the Sobel operator, which means it uses the 3×3 kernel. With the kernel details, image left–right adjustment points and upper–lower limit pixels are estimated to identify the edge relevant information. This process eliminates the edge information and smoothens the edge information, which causes to improve the overall ROI segmentation process. Here, the edges are investigated according to the horizontal and vertical direction. Therefore, the horizontal D_{h} is estimated by convoluting the two kernel values with the original image $D_{\mathrm{h}} = \begin{bmatrix} +1 & 0 & -1 \\ +1 & 0 & -1 \\ +1 & 0 & -1 \end{bmatrix} \times \mathrm{Img}$. Then the vertical D_{v} approximation values are estimated by convoluting the kernel value with the original image $D_{\mathrm{v}} = \begin{bmatrix} +1 & +1 & +1 \\ 0 & 0 & 0 \\ -1 & -1 & -1 \end{bmatrix} \times \mathrm{Img}$. After computing the two-directional approximation derivatives, the Prewitt kernel value is calculated for gradient smoothing $\begin{bmatrix} +1 & 0 & -1 \\ +1 & 0 & -1 \\ +1 & 0 & -1 \end{bmatrix} = \begin{bmatrix} 1 \\ 1 \\ 1 \end{bmatrix} [+1 \quad 0 \quad -1]$. Along with this, edge directional changes are computed as $D = \sqrt{{D_{\mathrm{h}}}^2 + {D_{\mathrm{v}}}^2}$ The estimated gradient approximation values are concatenated to get the edge magnitude value calculated using equation (6).

$$\Theta = a \tan 2(D_{\mathrm{h}}, D_{\mathrm{v}}) \tag{6}$$

From the computed magnitude orientation, the edge gradient direction value should be estimated according to equations (7 and 8).

$$D_{\mathrm{h}} = \frac{\partial f(h, v)}{\partial_{\mathrm{h}}} = f(h+1, v) - f(h, v) \tag{7}$$

$$D_{\mathrm{v}} = \frac{\partial f(h, v)}{\partial_{\mathrm{v}}} = f(h+1, v) - f(h, v) \tag{8}$$

The computed edge gradient direction value, derivatives of gradient, and vector gradient values are estimated as $\mathrm{grad}(f(h, v)) = [D_{\mathrm{h}},\ D_{\mathrm{v}}]^T = \left[\frac{\delta f}{\delta h},\ \frac{\delta f}{\delta v}\right]$. This has been written as

$$|\mathrm{grad}(f(h, v))| = \sqrt{{D_{\mathrm{h}}}^2 + {D_{\mathrm{v}}}^2} \tag{9}$$

Finally, the computed values are examined to predict the gradient direction $\delta(h, v) = \arctan\left[\frac{D_{\mathrm{h}}}{D_{\mathrm{v}}}\right]$. According to the Prewitt kernel values, image edge-relevant details are extracted. Similar edge information is grouped. This Prewitt kernel extracted process is applied continuously to the images for extracting the affected regions.

3.3 DBN-based feature derivation

The third important step is feature extraction, which is done by applying the cat swarm optimization algorithm-based deep belief network (CSA-DBN). The extracted edge regions are fed as the input to this process, and the meaningful features are derived. The DBN approach works according to the multilayer restricted Boltzmann machine (RBN) approach that extracts the in-depth image features. During this process, the input data and first hidden layers related to the probability distribution value are estimated in the visible layer computed via equation (10).

$$P(v, h^1, h^2, \ldots . h^n) = \left(\sum_{k=0}^{n-2} P(h^n | h^{n+1})\right) P(h^{n-1}, h^n) \tag{10}$$

The joint probability distribution (h^{n-1}, h^n) between visible and hidden layer values is computed from the RBN model's topmost layer. The RBN has two layers: a visible or input layer and a hidden layer, as shown in Figure 3. The RBN has the connection between the entire visible layer and hidden layer but having no

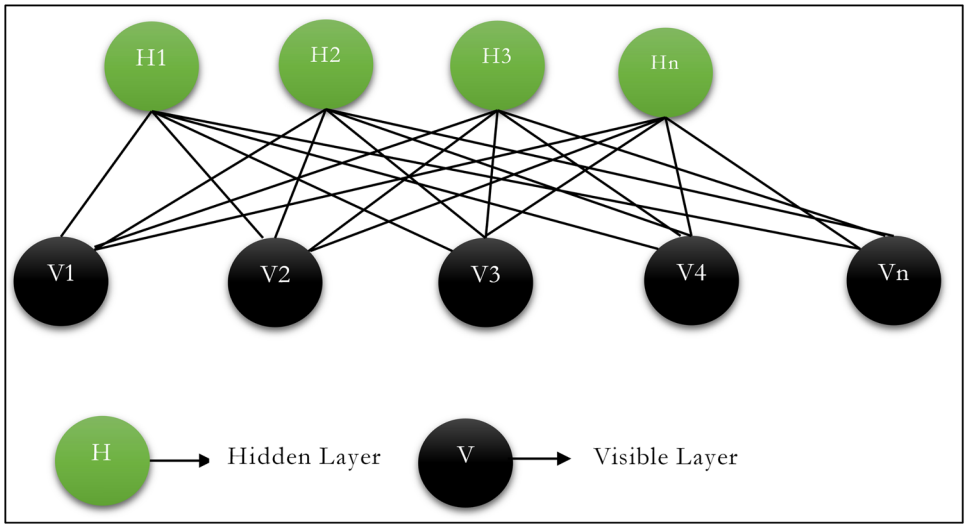

Figure 3: RBN structure.

connection within the layer and no connection between the invisible and visible layers. Then the probability distribution of hidden and visible layers is defined as $p(v, h)$ here; input image features are obtained from the output layer h. According to the discussion, $p(v, h)$ is estimated using equation (11a) and (11b).

$$p(v, h) = \frac{1}{Z(\theta)} \exp(-E(v, h)), \tag{11a}$$

$$p(v, h) = \frac{1}{Z(\theta)} \prod_{ij} e^{W_{ij} v_i h_j} \prod_i e^{b_i v_i} \prod_j e^{c_j h_j}. \tag{11b}$$

The $p(v, h)$ value is estimated from the network energy function $E(v, h)$ and the normalization factor $Z(\theta)$, which are derived from equation (11c) and (11d).

$$E(v, h) = -b'v - c'h - h'Wv, \tag{11c}$$

$$Z(\theta) = \sum_{h,v} \exp(-E(v, h)). \tag{11d}$$

Here, h and v denoted as hidden and visible layer units, visible and hidden layer connections are having W weight, c' is the hidden layer bias value, and b' is the visible layer bias value. After computing the $p(v, h)$ value, the network needs to be trained according to the learning parameters such as weight (W) and a bias value. Initially, the RBM network first layer was trained by fixed training parameters, and the output is passed to the next layer (hidden layer) to predict the image features. The last layer of the network utilizes the SoftMax regression function with supervised gradient descent algorithm. According to RBM algorithm, the training process is performed that helps to investigate the new medical images. In the training process, input samples are analyzed by computing the $p(v, h)$ value and contrast divergence value of learning parameter that is calculated as follows:

$$W = W + \varepsilon(h_1 x_1' - Q(h_2 = 1|x_2)x_2'), \tag{12}$$

$$b = b + \varepsilon(x_1 - x_2), \tag{13}$$

$$c = c + \varepsilon(h_1 - Q(h_2 = 1|x_2)). \tag{14}$$

Here, W is weight value, the learning rate of contrast divergence process is denoted as ε, and x_1, x_2 is denoted as the input vectors in the training process. The computed values belong to 1. The samples are trained effectively; the learning parameters should be converged. It has to be updated to improve the overall image training process. In the testing process, the last layer's output is fed into the SoftMax regression

function to estimate the image's features. During the input vector training process, AdaDelta learning process is utilized to minimize the convergence value. It is worked according to the squared delta's exponential moving average value. The new weight value is estimated by taking the difference between the newly updated weight value and current value. Therefore, the learning parameter values are replaced by the computed delta value. Then the new weight value is estimated using equation (15).

$$w_{t+1} = w_t - \frac{\sqrt{D_{t-1} + \varepsilon}}{\sqrt{v_t + \varepsilon}} \cdot \frac{\partial L}{\partial w_t}. \tag{15}$$

After computing the AdaDelta value, the RBM network trained again to improve the system's overall performance. Further, the current weight value detection process should be enhanced by applying the cat swarm optimization algorithm (CSA). The CSA algorithm works better than other optimization algorithms and can resolve the optimization problem during input training and classification. This algorithm works according to food searching behavior of cat, such as seeking and tracing mode. Initially, the cat investigates the surroundings and passes to the next position in the seeking mode. In the tracing process mode, the cat chases a specific target by identifying the location. The cat identifies the global solution in the seeking mode and the local solution in the tracking mode from the searching process. The cat has the seeking memory pool, mixed ratio, and dimension change count parameters during the searching process. In this process, the fitness value is computed for entire candidate points, and the most relevant probability values are chosen as the fitness value. Else, the seeking and tracking probability value is calculated to select the candidate value, which is done by equation (16).

$$P_k = \frac{\mathrm{FS}_k - \mathrm{FS}_b}{\mathrm{FS}_{\max} - \mathrm{FS}_{\min}}. \tag{16}$$

The seeking mode probability value P_k is computed from the fitness value, and the velocity of the cat chasing process is estimated in tracking mode using equation (17).

$$v_{k,d} = \beta \times v_{k,d} + c \times r_1 \times (x_{\mathrm{best},d} - x_{k,d}). \tag{17}$$

Here, d is the dimension, and position of the prey or weight value is estimated as $x_{k,d} = x_{k,d} + v_{k,d}$. Inertia weight values are denoted as β, the constant acceleration value is c, and r_1 represented as the random value from 0 to 1. The present and global positions are indicated, respectively, as $x_{k,d}$ and $x_{\mathrm{best},d}$. This process is repeated every time during the image analysis because the right selection and updating of weight value minimize the deviations while extracting features from the image. Then the overall working process of CSA-DBN-based image feature extraction process is illustrated in Figure 4.

Figure 4 shows that the region segmented image pixels are transmitted as the input represented as T1, T2, T3 ... Tn. The network processes the input pixels, and the output is obtained as

$$y(n) = \varphi(T(n) \times W^T(n)). \tag{18}$$

The computed output features are compared with the desired characteristics for investigating the error value done according to equation (19).

$$e(n) = d(n) - y(n). \tag{19}$$

If the network produces the error value, then the optimized weight values are selected according to the CSA optimization algorithm process. The algorithm fitness value is estimated using equation (20).

$$\mathrm{FS} = d(n) - \varphi((n) \times W^T(n)). \tag{20}$$

The new velocity is computed using equation (17), and the latest weight value is calculated based on the fitness function. The identified weight values are compared with the current weight value defined in equation (15), and the delta value is used to update the process. This process is repeated until the optimized features from the medical images are extracted. The extracted features are further examined by optimized classifiers such as DL techniques or other classifiers to recognize the affected region's condition. This

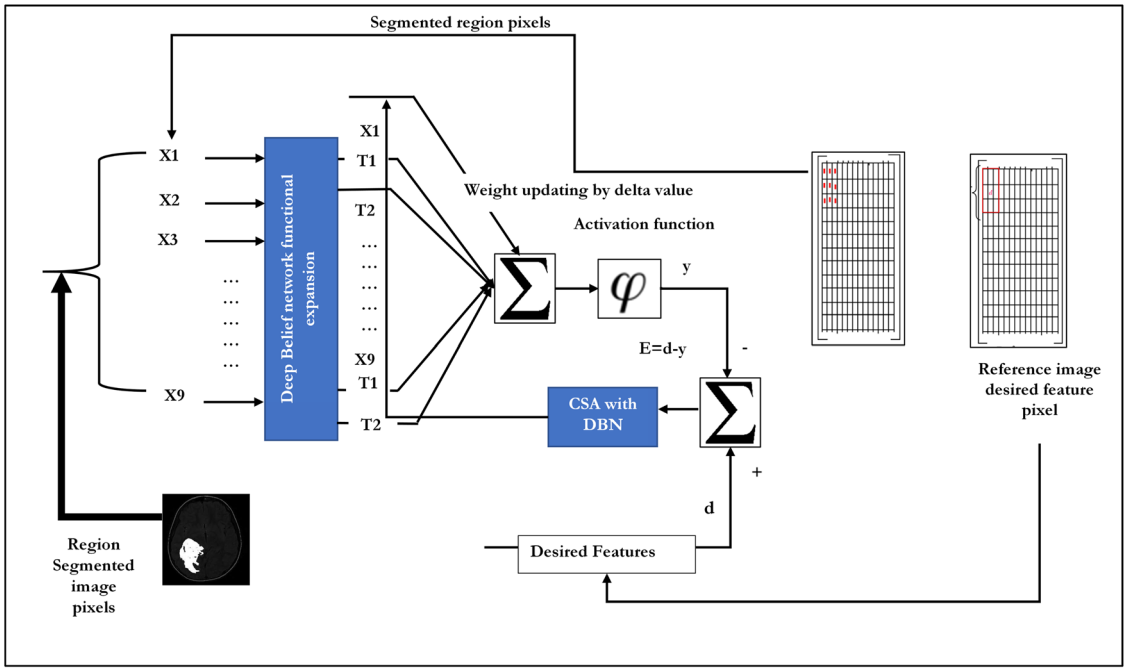

Figure 4: Structure of CSA-DBN feature extraction process.

process effectively identifies the radiographic image's deviation due to the effective examination of each image pixel.

4 Results and discussion

This section examines the effectiveness of the CSA-DBN-based radiographic image analysis process. The discussed system uses the Medical Segmentation Decathlon dataset for evaluating the proficiency of a defined system. The dataset consists of several radiographic images like hepatic vessel, prostate, liver, heart, brain tumor, spleen, pancreas, and colon. For every medical image, the massive number of radiographic details is illustrated in Table 2.

These medical images' segmented regions are investigated pixel by pixel in CSA-DBN algorithm for extracting the optimized features. The derived features are utilized to further image analysis by various

Table 2: Dataset description

Medical imaging	Images	Training	Testing
Liver tumor	201-3D images	131	70
Brain tumor	750-3D images	484	266
Hippocampus	394-3D volume	263	131
Lung tumor	96-3D images	64	32
Prostate	48-4D volumes	32	16
Cardiac	30-3D images	20	10
Pancreas tumor	420-3D images	282	139
Colon cancer	190-3D images	126	64
Hepatic vessels	443-3D images	303	140
Spleen	61-3D images	41	20

postimage processing techniques. The efficiency of the created system is determined using the following performance metrics:
Accuracy rate:

$$\text{Acc} = \frac{\text{TrPo} + \text{TrNe}}{\text{TrPo} + \text{TrNe} + \text{FaPo} + \text{FaNe}}, \tag{21}$$

$$\text{Recall (Rec)} = \frac{\text{TrPo}}{\text{TrPo} + \text{FaPo}}. \tag{22}$$

Precision rate:

$$\text{Pre} = \frac{\text{TrPo}}{\text{TrPo} + \text{FaPo}}, \tag{23}$$

F-score:

$$f_1 = \frac{2 \times \text{Pre} \times \text{Rec}}{\text{Pre} + \text{Rec}}. \tag{24}$$

In equations (21), (22), and (23), TrNe represents the true-negative rate, TrPo represents the true-positive rate, FaPo indicates a false-positive rate, and the FaNe indicates a false-negative rate.

The medical image's features are examined effectively from the computation of accuracy in equation (21). The CSA-DBN technique obtained results are compared with the existing research studies such as a DLA [24], TLDLF [26], MCRNN [28], and DRNN [30]. The obtained feature extraction accuracy (Acc) value is shown in Figure 5.

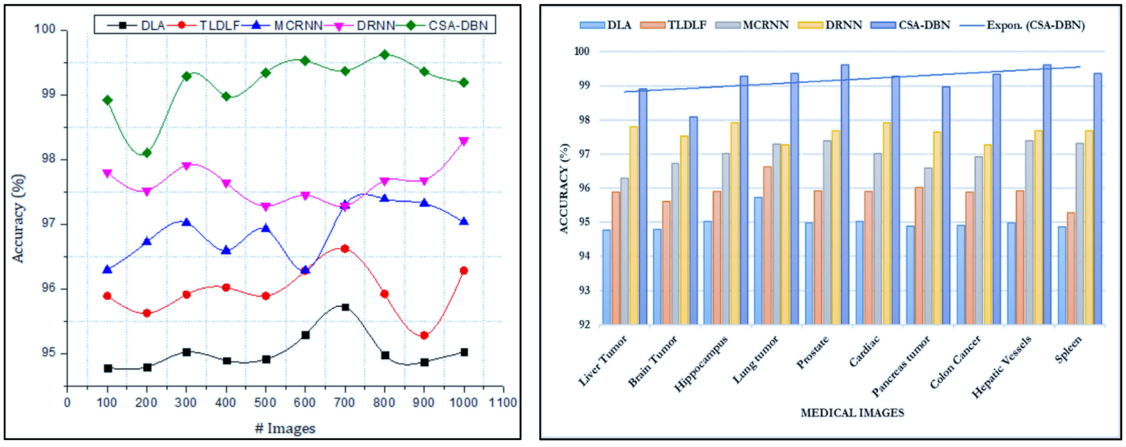

Figure 5: Accuracy analysis: (a) # images and (b) different images.

Figure 5 illustrated that the Acc value of various medical image analysis methods. Here the accuracy is determined in terms of the different number of images and the various medical images. The introduced CSA-DBN approach successfully examines the segmented image region pixels, and the effective features are extracted with maximum accuracy. The method computes the image features according to the convergence diverge learning parameter (W, b, and c), and probability distribution value of the hidden and visible layers is $p(v, h)$. The introduced method continuously examines the deviation between the computed and desired image features $e(n) = d(n) - y(n)$, which helps to update the network performance. Therefore, the introduced CSA-DBN approach ensures the high accuracy (99.32%) value collated with existing methods such as DLA(95.17%), TLDLF(95.91%), MCRNN(96.89%), and DRNN (97.94%). The accuracy value indicates that the

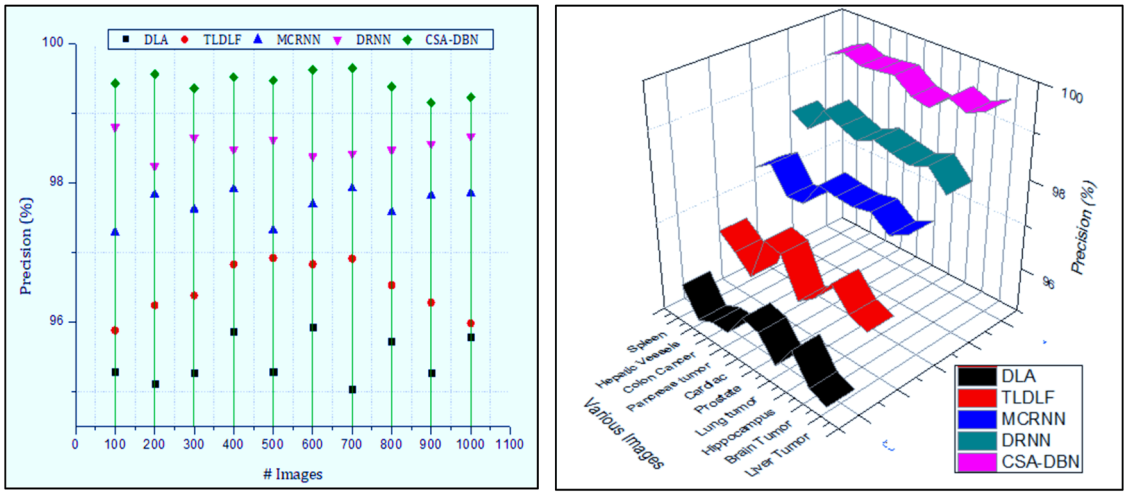

(a) (b)

Figure 6: Precision analysis: (a) # images and (b) different images.

introduced CSA-DBN approach derives the disease-related features from the Prewitt kernel-based segmented region. In addition to these metrics, the presented method's precision value should be examined on the different number of images and another type of medical images. The obtained results are illustrated in Figure 6.

Figure 6 illustrated the precision value of various medical image analysis methods. Here the precision values are investigated in terms of the different number of images and the various medical images. The CSA-DBN approach recognizes each pixel characteristics in hidden and visible layers according to the probability distribution function. Based on the $p(v, h)$ value, the network has been trained, and the delta values are used to update the network weight value. Due to the effective computation of pixel characteristics, the affected region-related features are extracted with the help of desired features in the training set. Hence, the introduced CSA-DBN approach ensures the high precision (99.22%) value collated with existing approaches such as DLA (95.67%), TLDLF (96.18%), MCRNN (96.9%), and DRNN (98.21%). The CSA-DBN approach not only recognizes the entire feature but also selects the right features from the extracted feature list. The obtained recall values are illustrated in Figure 7.

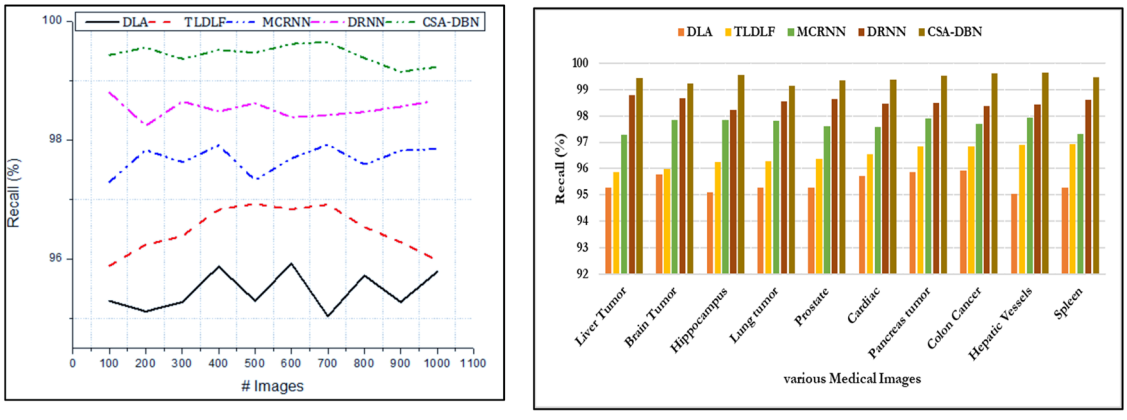

(a) (b)

Figure 7: Recall analysis: (a) # images and (b) different images.

Figure 7 illustrated the recall values of various medical image analysis methods. Here, the recall values are investigated in terms of the different number of images and the various medical images. The disease-related optimized features are selected from the extracted features according to the CSA seeking and tracking mode. The algorithm determines the best features by computing the fitness value-related weight-updating process. Hence, the introduced CSA-DBN approach ensures the high recall (99.41%) value collated with existing methods such as DLA (95.93%), TLDLF (96.23%), MCRNN (97.01%), and DRNN (98.25%). Due to the effective retrieval and selection of features, improves the overall image feature extraction process. Then the obtained *F*1-score values are illustrated in Table 3.

Table 3: *F*1-score

S. no	Methods	Training	Testing	Overall accuracy (%)
1	DLA [24]	96.83	96.13	96.48
2	TLDLF [26]	97.28	96.72	97
3	MCRNN [28]	97.92	97.38	97.65
4	DRNN [29]	98.28	98.13	98.205
5	CSA-DBN	99.24	99.41	99.325

Table 3 clearly shows that the CSA-DBN obtained high feature extraction accuracy (99.32%) compared to existing researchers works DLA (96.48%), TLDLF (97%), MCRNN (97.65%), and DRNN (98.20%). Although these methods attain high accuracy values, the introduced CSA-DBN approach has a minimum deviation value, which means the extracted features are almost the same as the desired image features. This effectiveness is evaluated using the error rate value. The obtained result is illustrated in Figure 8.

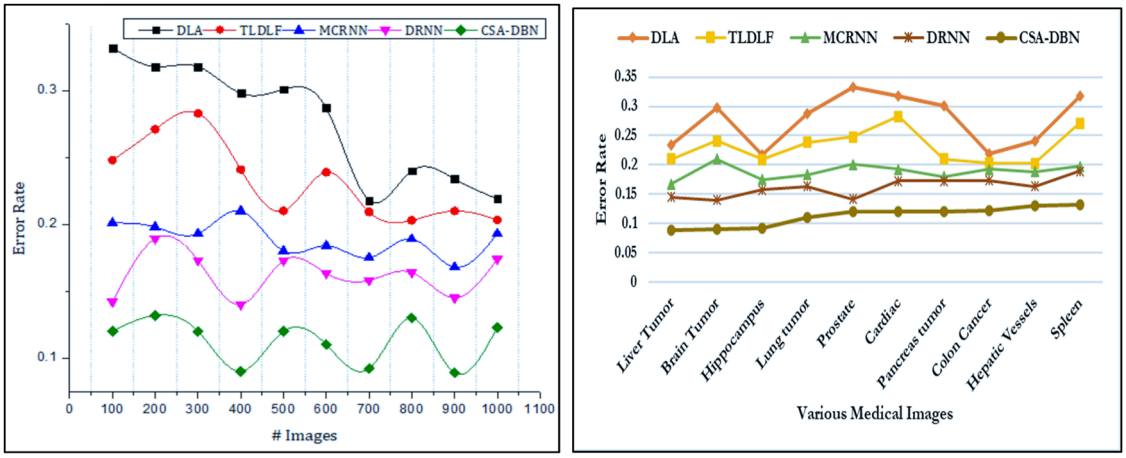

(a) **(b)**

Figure 8: Error value analysis: (a) # images and (b) different images.

Figure 8 illustrated the error values of various medical image analysis methods. The effective utilization of the seeking mode and tracing mode processes defined in CSA helps in selecting the correct weight value. Moreover, the chosen weight values are further examined $w_{t+1} = w_t - \frac{\sqrt{D_{t-1}+\varepsilon}}{\sqrt{v_t+\varepsilon}} \cdot \frac{\partial L}{\partial w_t}$, which causes to minimize the deviation between predicted and desired image features. Among the several approaches, CSA-DBN attains the minimum error value (0.11) compared to other methods. Thus, the introduced system successfully recognizes the disease-affected region-related features using optimized learning and training parameters.

5 Conclusion

Thus, the study analyzes the CSA-DBN-based radiographic image analysis process. In this study, the Medical Segmentation Decathlon dataset was utilized for gathering the medical images. The images are decomposed into approximation and detailed coefficient, which helps remove the noise from the image. Then the KSt test has been conducted to determine the similarity between the pixels. According to the value, the deviated pixels are computed and removed from the image. Then the Prewitt kernel operators are applied to identify the disease-affected region fed into the DBN. The DBN approach recognizes image features by utilizing the AdaDelta learning process. Further, the network process improved by updating the new weight value computed according to the cat swarm optimization technique's seeking and tracking mode. This effective process minimizes the deviation and enhances the feature detection accuracy up to 99.32%. In the future, the excellence of the system is enhanced by using meta-heuristic optimization algorithm based postradiographic image analysis.

Acknowledgements: We would like to thank Dijlah University College for funding this research.

Funding information: This research was supported by the Dijlah University College l [grant number G2021-1].

Conflict of interest: Authors state no conflict of interest.

References

[1] Wang C-W, Huang C-T, Lee J-H, Li C-H, Chang S-W, Siao M-J, et al. A benchmark for comparison of dental radiography analysis algorithms. Med Image Anal. 2016;31:63–76.
[2] Little KJ, Reiser I, Liu L, Kinsey T, Sánchez AA, Haas K, et al. Unified database for rejected image analysis across multiple vendors in radiography. J Am Coll Radiol. 2017;14(2):208–16.
[3] Malarvel M, Sethumadhavan G, Bhagi PCR, Kar S, Saravanan T, Krishnan A. Anisotropic diffusion based denoising on X-radiography images to detect weld defects. Digital Signal Process. 2017;68:112–26.
[4] Wang L, Lin ZQ, Wong A. Covid-net: a tailored deep convolutional neural network design for detection of covid-19 cases from chest X-ray images. Sci Rep. 2020;10(1):1–12.
[5] Mohammed MA, Ali IR, Obaid OI. Diagnosing pilgrimage common diseases by interactive multimedia courseware. Baghdad Sci J. 2022;19(1):168.
[6] Hussein IJ, Burhanuddin MA, Mohammed MA, Benameur N, Maashi MS, Maashi MS. Fully-automatic identification of gynaecological abnormality using a new adaptive frequency filter and histogram of oriented gradients (HOG). Expert Syst. 2021;e12789.
[7] Zokaeinikoo M, Kazemian P, Mitra P, Kumara S. Aidcov: an interpretable artificial intelligence model for detection of covid-19 from chest radiography images. medRxiv. 2020.
[8] Toussie D, Voutsinas N, Finkelstein M, Cedillo MA, Manna S, Maron SZ, et al. Clinical and chest radiography features determine patient outcomes in young and middle-aged adults with COVID-19. Radiology. 2020;297(1):E197–206.
[9] Kermany DS, Goldbaum M, Cai W, Valentim CCS, Liang H, Baxter SL, et al. Identifying medical diagnoses and treatable diseases by image-based deep learning. Cell. 2018;172(5):1122–31.
[10] Zhu H, Wang L, Fang C, Peng S, Zhang L, Chang G, et al. Clinical analysis of 10 neonates born to mothers with 2019-nCoV pneumonia. Transl Pediatrics. 2020;9(1):51.
[11] Dallora AL, Anderberg P, Kvist O, Mendes E, Ruiz SD, Berglund JS. Bone age assessment with various machine learning techniques: a systematic literature review and meta-analysis. PLoS One. 2019;14(7):e0220242.
[12] Cho BH, Kaji D, Cheung ZB, Ye IB, Tang R, Ahn A, et al. Automated measurement of lumbar lordosis on radiographs using machine learning and computer vision Global. Spine J. 2020;10(5):611–8.
[13] de Medeiros AD, Pinheiro DT, Xavier WA, da Silva LJ, dos Santos Dias DCF. Quality classification of *Jatropha curcas* seeds using radiographic images and machine learning. Ind Crop Products. 2020;146:112162.
[14] Lee SM, Seo JB, Yun J, Cho Y-H, Vogel-Claussen J, Schiebler ML, et al. Deep learning applications in chest radiography and computed tomography. J Thorac Imaging. 2019;34(2):75–85.
[15] Varma M, Lu M, Gardner R, Dunnmon J, Khandwala N, Rajpurkar P, et al. Automated abnormality detection in lower extremity radiographs using deep learning. Nat Mach Intell. 2019;1(12):578–83.

[16] Gu X, Pan L, Liang H, Yang R. Classification of bacterial and viral childhood pneumonia using deep learning in chest radiography. Proceedings of the 3rd International Conference on Multimedia and Image Processing; 2018. p. 88–93.
[17] Liang C-H, Liu Y-C, Wu M-T, Garcia-Castro F, Alberich-Bayarri A, Wu F-Z. Identifying pulmonary nodules or masses on chest radiography using deep learning: external validation and strategies to improve clinical practice. Clin Radiol. 2020;75(1):38–45.
[18] Paul HY, Kyung Kim T, Wei J, Shin J, Hui FK, Sair HI, et al. Automated semantic labeling of pediatric musculoskeletal radiographs using deep learning. Pediatric Radiol. 2019;49(8):1066–70.
[19] Baselice F, Ferraioli G, Pascazio V, Sorriso A. Denoising of MR images using Kolmogorov-Smirnov distance in a non local framework. Magnetic Reson Imaging. 2019;57:176–93.
[20] Zhang Y-D, Sui Y, Sun J, Zhao G, Qian P. Cat Swarm Optimization applied to alcohol use disorder identification. Multimed Tools Appl. 2018;77(17):22875–96.
[21] Sikkandar H, Thiyagarajan R. Deep learning based facial expression recognition using improved Cat Swarm Optimization. J Ambient Intell Humanized Comput. 2020;12(2):3037–53.
[22] http://medicaldecathlon.com/.
[23] Pandya MD, Shah PD, Jardosh S. Medical image diagnosis for disease detection: a deep learning approach. In U-Healthcare Monitoring Systems. United States: Academic Press; 2019. p. 37–60.
[24] Debelee TG, Schwenker F, Ibenthal A, Yohannes D. Survey of deep learning in breast cancer image analysis. Evol Syst. 2020;11(1):143–63.
[25] Wuestemann J, Hupfeld S, Kupitz D, Genseke P, Schenke S, Pech M, et al. Analysis of bone scans in various tumor entities using a deep-learning-based artificial neural network algorithm—evaluation of diagnostic performance. Cancers. 2020;12(9):2654.
[26] Rehman A, Naz S, Razzak MI, Akram F, Imran M. A deep learning-based framework for automatic brain tumors classification using transfer learning. Circuits Syst Signal Process. 2020;39:757–75. doi: 10.1007/s00034-019-01246-3.
[27] Sharma A, Kumar S, Singh SN. Brain tumor segmentation using DE embedded OTSU method and neural network. Multidim Syst Sign Process. 2019;30:1263–91. doi: 10.1007/s11045-018-0603-3.
[28] Abid MMN, Zia T, Ghafoor M, Windridge D. Multi-view convolutional recurrent neural networks for lung cancer nodule identification. Neurocomputing. 2021.
[29] Azizi S, Bayat S, Yan P, Tahmasebi A, Kwak JT, Xu S, et al. Deep recurrent neural networks for prostate cancer detection: analysis of temporal enhanced ultrasound. IEEE Trans Med Imaging. Dec. 2018;37(12):2695–703. doi: 10.1109/TMI.2018.2849959.
[30] Masud M, Eldin Rashed AE, Hossain MS. Convolutional neural network-based models for diagnosis of breast cancer. Neural Comput Applic. 2020. doi: 10.1007/s00521-020-05394-5.
[31] Chen H, Qi X, Yu L, Dou Q, Qin J, Heng PA. DCAN: deep contour-aware networks for object instance segmentation from histology images. Med Image Anal. 2017;36:135–46.
[32] Song Y, Tan EL, Jiang X, Cheng JZ, Ni D, Chen S, et al. Accurate cervical cell segmentation from overlapping clumps in pap smear images. IEEE Trans Med Imaging. 2017;36(1):288–300.
[33] Kumar N, Verma R, Sharma S, Bhargava S, Vahadane A, Sethi A. A dataset and a technique for generalized nuclear segmentation for computational pathology. IEEE Trans Med Imaging. 2017;36(7):1550–60.
[34] Ho DJ, Fu C, Salama P, Dunn KW, Delp EJ Nuclei detection and segmentation of fluorescence microscopy images using three dimensional convolutional neural networks. 2018 IEEE 15th International Symposium on Biomedical Imaging (ISBI 2018). IEEE; 2018: p. 418–22.
[35] Naylor P, Laé M, Reyal F, Walter T. Segmentation of nuclei in histopathology images by deep regression of the distance map. IEEE Trans Med Imaging. 2019;38(2):448–59.
[36] Zhou Y, Onder OF, Dou Q, Tsougenis E, Chen H, Heng PA. Cianet: Robust nuclei instance segmentation with contour-aware information aggregation. International Conference on Information Processing in Medical Imaging. Cham: Springer; 2019. p. 682–93.
[37] Xu Y, Li Y, Wang Y, Liu M, Fan Y, Lai M, et al. Gland instance segmentation using deep multichannel neural networks. IEEE Trans Biomed Eng. 2017;64(12):2901–12.
[38] Eppenhof KAJ, Pluim JP. Error estimation of deformable image registration of pulmonary CT scans using convolutional neural networks. J Med Imaging. 2018b;5(2):024003.
[39] Ma K, Wang J, Singh V, Tamersoy B, Chang Y-J, Wimmer A, et al. Multimodal image registration with deep context reinforcement learning. International Conference on Medical Image Computing and Computer-Assisted Intervention. Berlin: Springer; 2017. p. 240–8.